Multiphase-flow Statistics using 3D Detection and Tracking Algorithm (MS3DATA): Methodology and application to large-scale fluidized beds

Multiphase-flow Statistics using 3D Detection and Tracking Algorithm (MS3DATA): Methodology and Application to Large-Scale Fluidized Beds

A. Bakshi[a,*], C. Altantzis[a,b], R.B. Bates[a], A.F. Ghoniem[a]

[a] *Massachusetts Institute of Technology, Department of Mechanical Engineering*
77 Massachusetts Ave., Cambridge, MA 02139, USA
[b] *National Energy Technology Laboratory, Morgantown, WV 26507, USA*

Abstract

Bubble dynamics play a critical role in the hydrodynamics of fluidized beds and significantly affect reactor performance. In this study, MS3DATA (Multiphase-flow Statistics using 3D Detection And Tracking Algorithm) is developed, validated and applied to numerical simulations of large-scale fluidized beds. Using this algorithm, bubbles are detected using void fraction data from simulations and are completely characterized by their size, shape and location while their velocities are computed by tracking bubbles across successive time frames. A detailed analysis of 2D (across vertical sections) and 3D bubble statistics using 3D simulations of lab-scale (diameter 14.5 cm) and pilot-scale bed (diameter 30 cm) is presented and it is shown that the former (a) under-predicts sizes of larger bubbles, (b) cannot detect a large fraction of small bubbles (< 3 cm) and (c) is unable to track the azimuthal motion of bubbles in the larger bed. The scalability of the algorithm is discussed by comparing the computational cost of computing bubble statistics on highly resolved grids. Even though 3D bubble detection is significantly more expensive than 2D detection, the cost is still negligible compared to the cost of accurate simulations. Besides application to fluidization simulation data of large fluidized beds, this algorithm can be easily extended to characterize bubbles, droplets and clusters in other areas of multiphase flows.

Keywords: Multiphase flow, fluidized bed, Eulerian simulations, bubble dynamics, 3D statistics. large-scale detection and tracking

1. Introduction

Fluidized bed technology is one of the most employed paradigms of gas-solid flows in a variety of industrial applications including the energy, chemical, pharmaceutical and food and packaging industries and is especially suited for large-scale operations [1]. With ever increasing computational power complemented by the development of efficient numerical techniques, Computational Fluid Dynamics (CFD) is expected to play a critical role in the design and optimization of fluidized bed operations. The insights gained from accurate numerical simulations are especially valuable at commercial-scales where experimental data is limited because of the difficulties with measurements in the harsh and difficult-to-access environment of solid-gas flow. One of the challenges with computational simulations, however, is to accurately characterize the fluidization hydrodynamics using metrics which are both reliable and scalable.

Because of the limitations in conventional experimental measurement techniques, most fluidized beds in the past have been characterized using global parameters, temporally and/or spatially averaged, such as the solids holdup and pressure drop. In a recent study, Bakshi et al [2] focused on the influence of the solids-gas drag model and wall boundary condition on accuracy of fluidization predictions. The study demonstrated that these global parameters do not comprehensively describe the fluidization hydrodynamics. In fact, it was observed that changing the wall boundary condition, in terms of the specularity coefficient, did not affect the cross-section averaged solids hold-up, or the pressure drop, but resulted in significantly different gas-solids distribution and fluidization characteristics. More specifically, it has been shown, for both cylindrical [2] and thin rectangular beds [3], that solids circulation and bubble dynamics are essential metrics for describing the hydrodynamics including the solids and gas motion in the bed. This is particularly important in the context of

*Corresponding Author
Email address: abakshi@mit.edu, Telephone number: +1 (617) 253-5365

reactive fluidization where reactor performance may be optimized based on the residence times of gas volatiles and solid fuel. Solids circulation is indicative of the solids mixing time within the bed. However, it can only be measured using tracer particles or through direct optical access, limiting measurements to thin lab-scale beds. In the meantime, both experimental [4–9] and numerical [2, 3, 10–12] studies conclude that solids motion is driven by bubble motion. However, a validated correlation linking these two has not been established due to the lack of experiments simultaneously measuring the solids and bubble motion, for a range of particle properties and operating conditions. Thus, predicting bubble dynamics accurately using validated numerical simulations and carefully identifying the bubble characteristics in the simulation results will not only describe the bubble distribution and motion reliably, but also provide valuable insights into the solids motion in the bed.

Recognizing the importance of bubble dynamics, there have been several experimental studies focused on characterizing bubbles in fluidized beds, including their size, location, shape (or aspect ratio) and velocity. In thin rectangular beds, these statistics have been obtained using high speed cameras and digital image analysis [13–15]. In cylindrical beds, however, such optical accessibility is not possible and bubbles are detected and characterized using intrusive or sophisticated non-intrusive techniques. In the past, probes have been inserted in the bed at different radial and axial locations which detect bubble passage by means of optical signals [16, 17], pressure fluctuations [18–20] or electrical pulses [21, 22]. Additionally, several researchers [18–20] have also attempted to correlate optical signals with pressure fluctuations for different particles and fluidization regimes, using characteristic length scales based on the particle-gas properties and local bubble diameter. Meanwhile, sophisticated non-intrusive measurement techniques have been developed recently including X-Ray [23–26], electrical capacitance [23] and MRI [27]. While these techniques offer high spatial and temporal resolution and can reconstruct the three-dimensional profile of bubbles, their application to large-scale fluidized beds is restricted by technical limitations.

Bubble statistics derived from numerical simulations of fluidized beds have been largely restricted to 2D, either applied directly to thin rectangular beds (e.g. [3, 28, 29]) or to cylindrical beds by analyzing vertical or cross-sectional slices (e.g. [2, 25]) of the bed. When applied to simulation data from 3D lab-scale beds, 2D bubble statistics suffice because bubble growth and coalescence are aided by the walls and larger bubbles eventually move upwards through the reactor center [30]. Thus, bubble statistics using either approach (vertical or cross-sectional slices) reveal similar trends [2]. However, this approach may not be applicable to larger beds because a large fraction of small bubbles remains undetected and azimuthal tracking is infeasible using simulation data along vertical sections only. Recently, Lu et al [29] developed flood-fill method (in 2D but can be extended to 3D) which checks neighbors of every cell and uses *target-grid* and *pending-grid* sequences to keep track of and identify bubble boundaries. Similarly, Sobrino et al [31] implemented 3D bubble detection by sectioning the bed horizontally at different axial locations, evaluating the bubble centroids at each cross-section and then stacking the 2D contours in consecutive horizontal sections to reconstruct the 3D bubble profile. While accurate, these approaches may be inefficient when applied to large volumes of simulation data from pilot/commercial-scale beds. An accurate and efficient 3D bubble detection algorithm is required to characterize the distribution and motion of bubbles in large-scale beds. This tool will also be essential for cases of asymmetric fluidization (e.g. [32, 33]) and can be easily extended to other areas of multiphase flow for characterizing bubbles, clusters and/or droplets and validating 3D numerical simulations directly [34–42].

This work is part of a series of studies focused on accurately predicting fluidization in large-scale reactors. In previous studies [2, 3, 43], physical and numerical models have been extended and validated by comparing solids circulation and bubble dynamics with several independent experimental measurements on lab-scale setups. Bubble statistics in these studies are based on 2D detection and linking, an approach which does not suffice at large scales, as also shown later in this study. Thus, this study is focused on the development of MS3DATA (Multiphase-flow Statistics using 3D Detection And Tracking Algorithm) applied to dense solid-gas flows for accurately and efficiently computing bubble statistics in 3D. A detailed description of the methodology is presented in Section 2, first in 2D for ease of illustration and then its extension to 3D. The methodology is validated in Section 3.1 using a combination of analytical shapes as well as experimental data from bubbling fluidized beds and subsequently applied to large-scale bed simulation data in Section 3.2. The simulation setup here is identical as previously presented in [2], with the exception that bubble detection in this study is based on 3D void fraction data from simulations while the previous study was restricted to 2D detection using image visualization. Limitations of existing 2D statistics (with respect to accurate 3D statistics) are highlighted in Section 3.3 and finally, the algorithm scalability is discussed in Section 3.4. While some details regarding the theoretical and numerical model for the simulations are discussed in Section 3, the specifics have been detailed previously in [2]. All simulations are conducted using MFiX (Multiphase Flow for Interphase Exchanges), an open-source code developed by the National Energy Technology Laboratory (NETL), USA while MS3DATA is

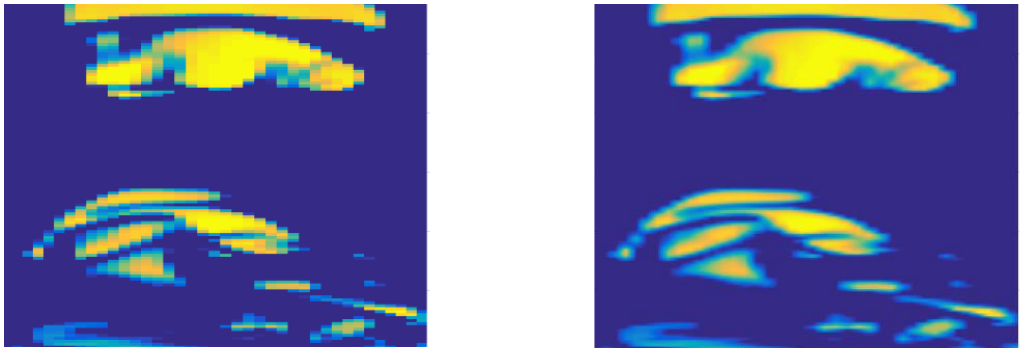

Figure 1: Snapshot of simulation results shown along a vertical section (2D) taken through the bed centerline (left) smoothed for evaluating bubble statistics (right). Selective thresholding is performed to highlight bubble boundaries (bubbles are colored in yellow).

developed in-house using commercial software MATLAB.

2. Methodology

The key steps for bubble detection are first discussed in 2D for illustration. These include data collection and interpolation in Section 2.1, and bubble detection and numbering in Section 2.2. The algorithm is extended to 3D and necessary modifications are highlighted in Section 2.3. The evaluation of bubble properties and linking of bubbles across successive frames are described in Sections 2.4 and 2.5 respectively.

2.1. Data Collection and Interpolation

To mitigate the impact of the volume of data required to examine statistically independent bubble dynamics, spatially resolved raw data is input to the algorithm by identifying cells using unique (global) cell indices rather than spatial coordinates. The bubble void threshold ϵ_g^b is the critical void fraction for bubble detection while the input void threshold ϵ_g^* ($< \varepsilon_g^b$) is used to filter out cells associated with void fraction less than ϵ_g^*. Thus, increasing ϵ_g^* increases the number of discarded cells thereby decreasing the computational cost for bubble detection, but may also affect the accuracy of bubble statistics since cells with void fraction $\epsilon_g > \epsilon_g^*$ are used for resolving bubble boundaries through interpolation. In this study, ϵ_g^b is set at 0.7 (based on [18]) while ϵ_g^* at 0.6. Such an approach reduces the transfer of data volume per frame significantly since a substantial fraction of the bed associated with the dense phase $\varepsilon_g < \varepsilon_g^*$ is not considered by the algorithm. The cell indices and corresponding void fraction data (for cells with $\varepsilon_g > \varepsilon_g^*$) are then used to recreate the spatially resolved void fraction field on MATLAB. Finally, the field is smoothed and interpolated on a fine grid (x_i, y_i) to accurately resolve bubble boundaries. For this study, a second-order interpolation scheme suffices, but could be set to higher accuracy based on the choice of interpolating function used (with increased computational cost). The final grid $\mathbf{A}$, subsequently used for bubble detection and linking, may, thus, be represented as

$$\mathbf{A} = [i,\, \mathrm{x}_i,\, \mathrm{y}_i,\, \varepsilon_{g,i}] \ni \varepsilon_{g,i} > \epsilon_g^*$$

where $\mathbf{A}$ is a matrix of size $n{\times}4$ with n grid cells and each cell i associated with coordinates (x_i, y_i) and void fraction $\varepsilon_{g,i}$. A representative illustration of the interpolation is shown in Figure 1. Note that without loss of generality, $\mathbf{A}$ is assumed in Cartesian format even though simulation data and the following discussion can be generally described in any grid (non-orthogonal / unstructured).

2.2. Bubble Detection

A schematic representation of $\mathbf{A}$ is shown in Figure 2a. Cells in $\mathbf{A}$ are linked together by checking the respective right and top neighbors i.e. if both cell i (x_i, y_i) and its right neighbor i_r ($\mathrm{x}_i{+}\Delta\mathrm{x}$, y_i) satisfy the bubble threshold criterion, i.e. $\varepsilon_{g,i} > \varepsilon_g^b$ and $\varepsilon_{g,i_r} > \varepsilon_g^b$, cell i_r gets linked to cell i (and likewise for the top neighbor i_t). Thus, the linked field can be described as

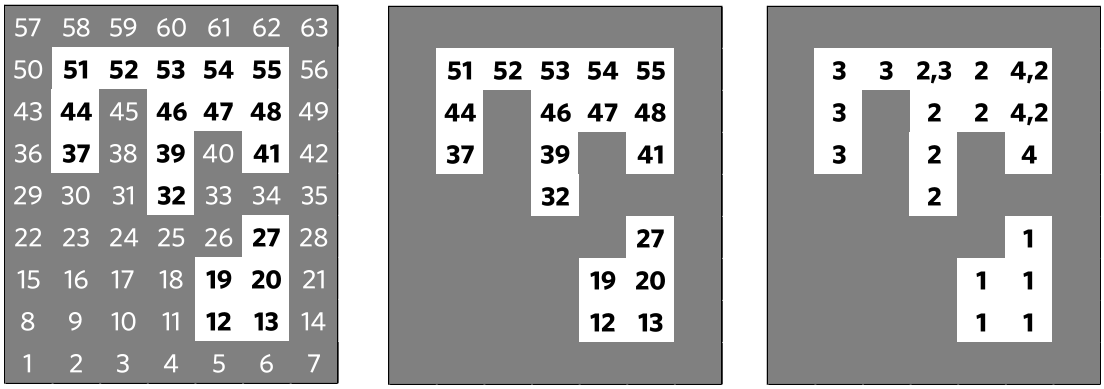

(a) Grid cell indexing (b) Eliminating cells with $\varepsilon_g < \varepsilon_g^b$ (c) Bubble numbering

Figure 2: Bubble detection in 2D (black text over white background indicates cells with $\varepsilon_g > \varepsilon_g^b$)

$$\mathbf{B_1} = [i,\ \mathrm{x}_i,\ \mathrm{y}_i,\ \varepsilon_{g,i},\ \delta_r i_r,\ \delta_t i_t]$$

$$\delta_r = \begin{cases} 1 \text{ if } \varepsilon_{g,i} > 0.7 \text{ and } \varepsilon_{g,i_r} > \varepsilon_g^b \\ 0 \text{ otherwise} \end{cases}$$

$$\delta_t = \begin{cases} 1 \text{ if } \varepsilon_{g,i} > 0.7 \text{ and } \varepsilon_{g,i_t} > \varepsilon_g^b \\ 0 \text{ otherwise} \end{cases}$$

where i_r and i_t represent the global indices of the neighbors of cell i (e.g. for i=46, i_r=47 and i_t=53). A schematic representation of $\mathbf{B_1}$ is shown in Figure 2b. As described in Algorithm 1, bubble numbering is a two-step process:

1. Determine bubble number bn_i for cell i; either pre-assigned (this is possible if cell i is linked previously) or set to the current value of bubble counter *nbubble*.
2. Link cells by assigning bn_i to i's neighbors i_r and i_t

Note that numbering conflicts could arise in Step 2 if the left and bottom neighbors are associated with different bubble numbers (e.g. cell 53 is linked to cell 52 to the left with bn_{52}=3 and cell 46 to the bottom with bn_{46}=2 in Figure 2c). If so, the conflicting number is recorded as $bn_{i_r,con}$ (i.e. bn_{53}=2 and $bn_{53,con}$=3 as linked from the bottom and left, respectively). Thus, the collection of points and their corresponding bubble numbers may be represented as:

$$\mathbf{B} = [i,\ \mathrm{x}_i,\ \mathrm{y}_i,\ bn_i,\ bn_{i,con}]$$

Algorithm 1: Bubble Numbering in 2D

```
nbubble = 1, bn_i = 0 ∀i ∈ B_1
for i ∈ B_1 do
    // Obtaining bubble number if previously unassigned
    if bn_i=0 then
        if δ_r i_r >0 and bn_{i_r} >0 then bn_i=bn_{i_r}
        else bn_i = nbubble, nbubble = nbubble+1
    // Neighbor linking
    if δ_r i_r >0 then
        if bn_{i_r}=0 then bn_{i_r} = bn_i
        else if bn_{i_r} ≠ bn_i then bn_{i_r,con} = bn_i
    if δ_t i_t >0 then bn_{i_t} = bn_i
```

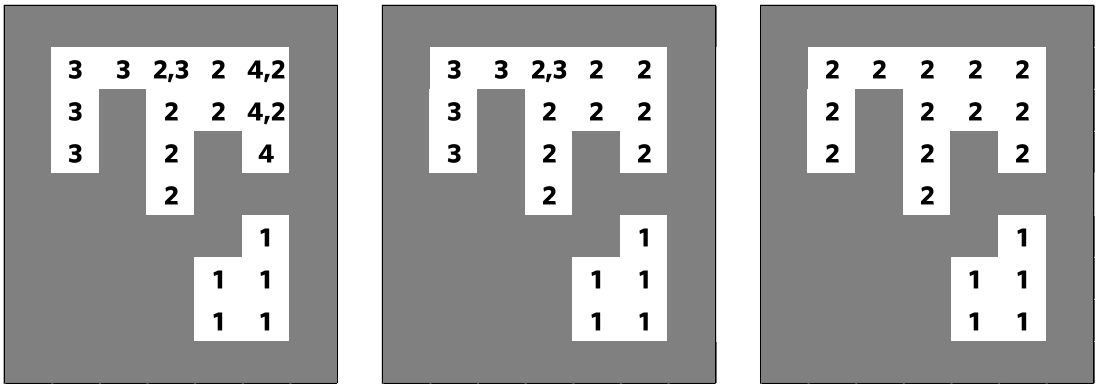

Figure 3: Recursive resolution of bubble conflicts in 2D based on Algorithm 2

Physically, these conflicts represent the set of bubbles that are identical since one grid cell can at most be associated with one bubble. Thus, the set of bubble numbering conflicts $\boldsymbol{C}$ (cases for which $bn_i \neq bn_{i,con}$) can be identified and bubble numbers can be recursively corrected using Algorithm 2 illustrated in Figure 3 where Bubbles 2, 3 and 4 are eventually reduced to one bubble. Once all conflicts in bubble numbering are resolved, the final collection of points and their associated bubble numbers is

$$\mathbf{D} = [i,\ \mathrm{x}_i,\ \mathrm{y}_i,\ bn_i]$$

so that each grid cell is associated with at most one bubble. Conversely, every bubble in the frame can be identified as a cluster of grid cells and properties can be evaluated based on the constituent cells. These properties are discussed in Section 2.4.

Algorithm 2: Resolving Bubble Conflicts

```
// C = set of unique conflict combinations
```
$C_j = (C_{j,1}, C_{j,2}) = (bn_j, bn_{j,con}) \forall j \ni bn_{j,con} > bn_j$

```
// Resolve bubble conflicts
```
n_{con} = number of conflicts (rows in **C**)
for $j = n_{con}$ to *1* **do**
  for $i \in \boldsymbol{B}$ **do**
    if $bn_i = C_{j,2}$ **then** $bn_i = C_{j,1}$
    if $bn_i > C_{j,2}$ **then** $bn_i = bn_i$-1

2.3. Extension to 3D

The algorithm discussed in Sections 2.1 - 2.2 can be extended to 3D by modifying **A** and **B** to include the added dimension. However, in this case, an extra bubble conflict could arise since any cell can be linked both from the left as well as the bottom, if the cells are indexed in the order x, y and then the depth z (added dimension). Thus, the collection of points with the respective bubble numbers is

$$\mathbf{B} = [i,\ \mathrm{x}_i,\ \mathrm{y}_i,\ \mathrm{z}_i,\ bn_i,\ bn_{i,con_1},\ bn_{i,con_2}]$$

For resolving bubble numbering conflicts, each conflicting row in **B** is broken down into two independent conflicts (bn_i, bn_{i,con_1}) and (bn_{i,con_1}, bn_{i,con_2}), the set of which can be resolved in a way similar to Algorithm 2. Because these matrices are large and simulation data is sampled at 100 Hz, all operations are carried out using parallel-looped vectorized equations in MATLAB.

2.4. Bubble Properties

Bubble properties are evaluated by considering the constituent cells forming every bubble. A centroid represents the average coordinates of the bubble and can be evaluated for the ith bubble bn_i as follows:

$$x_{c,i} = \frac{1}{n_{b,i}} \sum x_i \in bn_i \tag{1}$$

where $n_{b,i}$ is the total number of cells encapsulated by bubble i on the fine grid (and likewise $y_{c,i}$ and $z_{c,i}$). Next, the bubble equivalent diameter is defined based on the total volume $V_{b,i}$ of the bubble,

$$d_{b,i} = \sqrt[3]{\frac{6V_{b,i}}{\pi}} \qquad V_{b,i} = n_{b,i}\Delta x\Delta y\Delta z \tag{2}$$

so that $d_{b,i}$ represents the diameter of the sphere having the same volume as the bubble and $\Delta x\Delta y\Delta z$ is the grid cell volume. In 2D statistics, the area based bubble diameter may be defined similarly as $\sqrt{4A_{b,i}/\pi}$. Next, bubble extremities can be described by the cord length (CL_i), lateral span (L_{bx} or L_{bz}) and set of aspect ratios (AR_1 and AR_2) given by

$$CL_i = (max(y \in b_i) - min(y \in b_i))\,\Delta y \tag{3}$$

$$L_{bx,i} = (max(x \in b_i) - min(x \in b_i))\,\Delta x \qquad AR_{1b,i} = \frac{CL_i}{L_{bx,i}} \tag{4}$$

$$L_{bz,i} = (max(z \in b_i) - min(z \in b_i))\,\Delta z \qquad AR_{2b,i} = \frac{CL_i}{L_{bz,i}} \tag{5}$$

2.5. Bubble Velocity

To obtain bubble velocities, Lagrangian Velocimetry Technique (LVT) is applied to link bubbles across consecutive frames [2]. In this algorithm, bubbles are numbered in every frame based on their axial and lateral positions and velocities are computed by evaluating distance transversed by corresponding bubbles i.e. for bubble i across frames p and p+1, the bubble axial velocity is given by

$$v_{by,i} = \frac{y_{c,i}^{p+1} - y_{c,i}^{p}}{\Delta t} \tag{6}$$

and similarly for the lateral velocities $v_{bx,i}$ and $v_{bz,i}$. The radial and azimuthal bubble velocities can then be obtained using a simple transformation -

$$v_{br,i} = v_{bx,i}cos\theta + v_{bz,i}sin\theta \tag{7}$$

$$v_{b\theta,i} = -v_{bx,i}sin\theta + v_{bz,i}cos\theta \tag{8}$$

where θ denotes the azimuthal location. Finally, to prevent erroneous linking of bubbles due to coalescence and splitting, the following filters are imposed:

- Frames p and p+1 must have the same overall bubble count.
- Bubble axial (rise) velocity must be positive and less than the maximum expected value (based on bubble velocity correlation by Mori and Wen [44])
- The maximum bubble lateral velocity is hard-coded into the algorithm based on simulation visualizations due to lack of experimentally derived correlations (value depends on data sampling frequency).

Note that filters have been commonly used for linking bubbles, both in experimental and computational studies (e.g. [3, 14, 16, 29]). These filters ensure accurate and reliable tracking but must be based on case-specific multiphase-flow characteristics. For bubbling fluidization of Geldart B particles, this approach has been validated previously [2] and verified using 3D simulation visualizations for the present study. Finally, the set of properties for all bubbles can be described by (and not limited to)

$$\mathbf{E} = [\vec{\mathbf{x}}_{\mathbf{c,i}},\, d_{b,i},\, AR_{1b,i},\, AR_{2b,i},\, \vec{\mathbf{v}}_{\mathbf{b,i}}]$$

Time and cross-section averaged bubble statistics are obtained by binning bubbles (centroid) based on their axial locations. For any bubble property ϕ, the averaged property $\bar{\phi}$ at axial location y_j can then be obtained using

$$\bar{\phi}(y_j) = \frac{1}{N_j}\left(\sum \phi_i | y_{c,i} \in \left[y_{j-1/2}, y_{j+1/2}\right]\right) \tag{9}$$

where N_j is the total number of bubbles with centroid axial location $y_{c,i}$ within the axial bin $y_{j-1/2}$ and $y_{j+1/2}$. To obtain reliable and statistically independent properties, bubble velocities are obtained using simulation data corresponding to 27s of real time and sampled at 100 Hz (total 2700 frames).

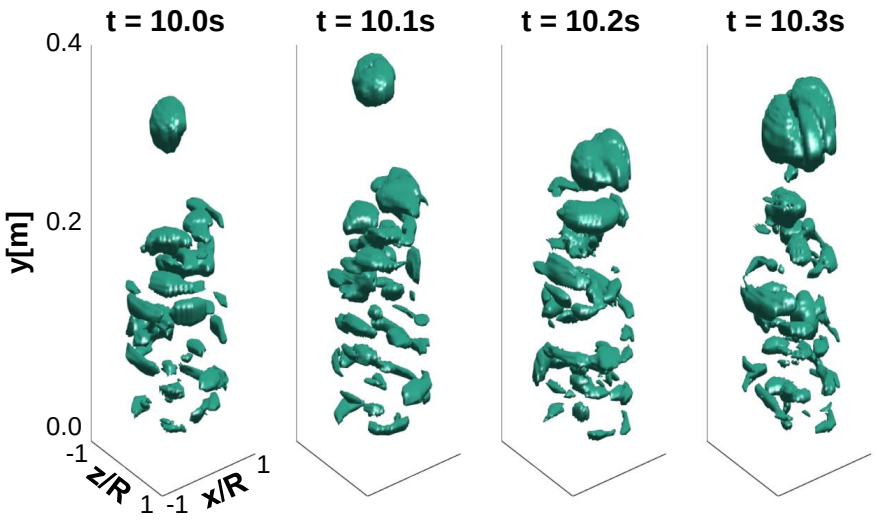

Figure 4: Typical time instant visualizations of bubbles in lab-scale bed (diameter = 14.5 cm) for U/U_{mf}=2.3. Void fraction threshold for bubble detection ε_g^b is 0.7.

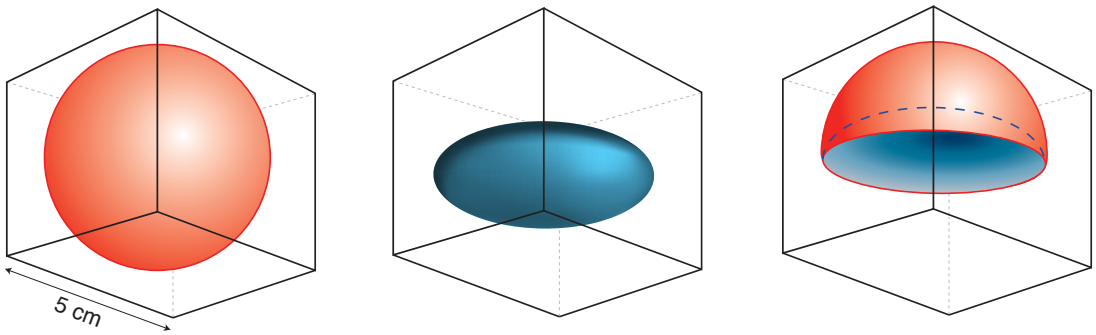

(a) (b) (c)

Figure 5: Analytical shapes considered for validation of MS3DATA: (a) Sphere (diameter 5 cm) (b) Ellipsoid (axes 5 cm × 5 cm × 2.5 cm) and (c) Composite formed by discounting ellispoid from sphere and halving. The computational domain is the circumscribing cube of length 5 cm.

3. Results and Discussion

In this study, 3D numerical simulations are performed using the Two-Fluid Model which describes the motion of both the gas and solid phases as continua. While this framework is computationally efficient, closure relationships are required for modeling particle-scale interactions. The inter-particle interactions are modeled using the solids stress tensor, which is evaluated using the frictional theory by Schaeffer [45] in dense regions of the bed and the Kinetic Theory of Granular Flow [46] in dilute pockets of the bed. Next, the gas-solids drag force is computed using Syamlal-O'Brien model [47] based on the previous study investigating the suitability of drag models in different regimes [2]. Finally, the particle-wall interactions are modeled using the Johnson-Jackson model [48], which evaluates the solids slip velocity at the walls by considering momentum and granular energy balance. These interactions are characterized by the specularity coefficient evaluated using the previously validated numerical expression by Li and Benyahia [2, 49]. Further details regarding the TFM, governing equations and numerical technique can be found in [47, 50].

All simulations are performed using MFiX, an open source code developed by NETL, USA for bubbling fluidized beds at two scales: lab-scale bed (LSB) of diameter 14.5 cm for validation and pilot-scale bed (PSB) of diameter 30 cm to highlight the advantages of 3D statistics. In order to describe the hydrodynamics accurately, highly resolved 3D cylindrical grids are used, with variable radial-grid resolution to ensure validity of solids continuum in cells close to the bed center (overall grid resolution is in the range 8-12 particle-diameters) [43].

Table 1: Volume predictions (in cm^3) using MS3DATA for typical bubble shapes illustrated in Figure 5. The circumscribing cube of side 5 cm is discretized using 200 cells in each dimension.

Shape	Volume	
	Analytical	Predicted
Sphere	65.450	66.445
Ellipsoid	32.725	33.219
Composite	16.362	16.611

Table 2: Grid cells for accurate bubble statistics; size($\mathbf{A}$) represents the number of cells in $\mathbf{A}$

Type	Bed ID×Ht [cm]×[cm]	Simulation Grid $N_r \times N_y \times N_\theta$	Framework (2D/3D)	size($\mathbf{A}$) $N_x \times N_y \times N_z$
Lab Scale (LSB)	14.5×60.0	20×120×12	3D	80×360×80
Pilot Scale (PSB)	30.0×60.0	40×120×20	2D	160×360×1
			3D	160×360×160

MS3DATA described in Section 2 is first validated in Section 3.1 and then, applied to large-scale fluidized bed to obtain time averaged statistics in Section 3.2. Next, a detailed comparison of 2D and 3D statistics applied to the 3D simulation data is presented in Section 3.3 and finally, scaling of the computational cost with different grid sizes is discussed in Section 3.4. Details on the grid size are presented in Table 2 while the simulation set-up is discussed in [2]. All bubble statistics are obtained using 2700 frames (27s real time at 100 Hz).

3.1. Validation

MS3DATA is validated rigorously by (a) using shapes with analytically determined volumes and (b) computing bubble statistics using previously validated fluidized bed simulations and comparing with experimental measurements and 2D statistics [2]. Typical bubble shapes (of size 5 cm) shown in Figure 5 are considered as test cases, including sphere (diameter 5 cm), ellipsoid (axes 5 cm × 5 cm × 2.5 cm) and a composite shape obtained by discounting the ellipsoid from sphere. The computational domain (circumscribing cube of side 5 cm) is discretized using different cell counts (10^3 - 200^3) corresponding to grid resolutions 0.25-5.00 mm. Next, the algorithm described in Section 2 is employed to compute bubble volumes considering only cells whose centers lie in the interior of the bubbles (test shapes). Table 1 shows that MS3DATA detects all three bubble shapes within 1.5% of the analytical solution. Further, Figure 6 illustrates that the prediction error decreases linearly with increasing resolution and using 1.5 mm-2 mm grids results in sufficiently accurate (within 10%) predictions. Note that the errors indicated here are in comparison with analytically derived expressions while simulation data is often obtained using grids coarser than 3-5 mm for bubbling fluidization of Geldart B particles ($\sim 10d_p$) [43] and error in experimental measurements is on the order of 20% [18]. Thus, prediction errors

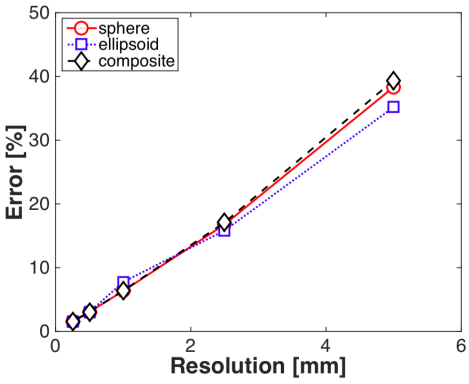

Figure 6: Error in volume prediction of bubbles shown in Figure 5 using computational grid of different resolutions

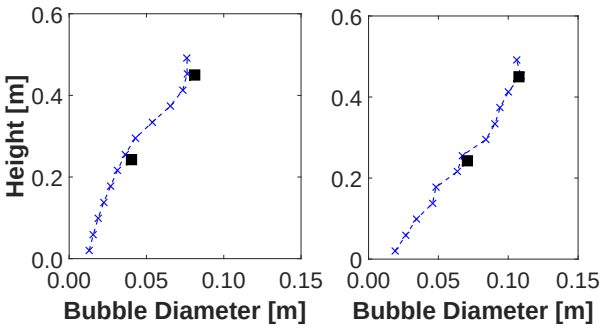

(a) U/U_{mf}=2.3 (b) U/U_{mf}=4.6

Figure 7: Comparison of average bubble diameter (cord length) from simulations using 3D bubble statistics for U/U_{mf}=2.3 and 4.6 with experimental measurements (*filled squares*) [18]

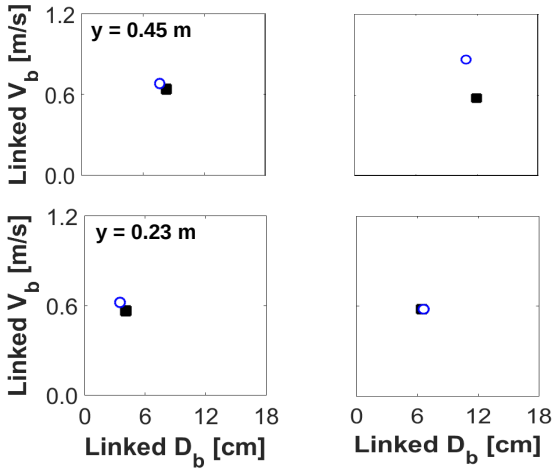

(a) U/U_{mf}=2.3 (b) U/U_{mf}=4.6

Figure 8: Comparison of average bubble velocity from simulations using 3D bubble statistics for U/U_{mf}=2.3 and 4.6 with experimental measurements (*filled squares*) [18]

in computing bubble dynamics may be rendered insignificant.

Next, MS3DATA is employed for computing bubble statistics using void fraction data from previously validated numerical simulations [2]. In [2], bubble dynamics were predicted using a combination of image visualization software (VisIt), ImageJ (http://imagej.nih.gov/ij/) and MATLAB, and compared to experimental measurements by Rüdisüli et al [18] to validate the wall boundary condition and gas-solids drag model. In the present study, all these steps have been generalized to 3D and integrated into a single MATLAB-based package MS3DATA based on time-instant data input from simulations. In [18], fluidization of alumina particles (average diameter 289 μm) is carried out in a 14.5 cm diameter glass fluidized bed for different inlet superficial gas velocities. Predictions of time-averaged bubble cord lengths using MS3DATA for two inlet gas velocities U/U_{mf} = 2.3 and 4.6, as shown in Figure 7, reveal excellent agreement with experimental measurements. As expected, small bubbles are formed close to the distributor coalescing to form larger bubbles higher up in the bed. Similarly, bubble velocity predictions shown in Figure 8 also predict experimental observations reasonably, although simulations seem to slightly over-predict the velocity for U/U_{mf} = 4.6 at y=0.45 m due to slugging effects at high velocities. Further, these statistics also show good agreement with 2D statistics shown in Figure 10 (computed previously in [2]) and the comparison is also discussed in Section 3.3.

3.2. Bubble Statistics in Large Fluidized Beds

In this section, bubble statistics are computed for the Pilot-Scale Bed (PSB) of diameter 30 cm. In these simulations, all operating conditions (particle properties, inlet gas velocity, other physical and numerical constants) are unchanged (compared to the lab-scale bed *LSB* of diameter 14.5 cm) to investigate the impact of bed diameter on the bubble dynamics. Figure 9 presents time-averaged bubble properties for the case of

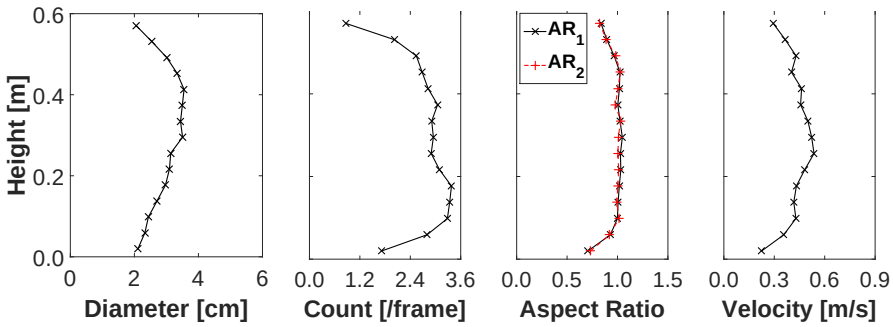

Figure 9: Bubble properties using the 3D algorithm applied to pilot-scale bed (diameter 30 cm) simulations for U/U_{mf}=4.6. Note that 'velocity' refers to bubble axial velocity.

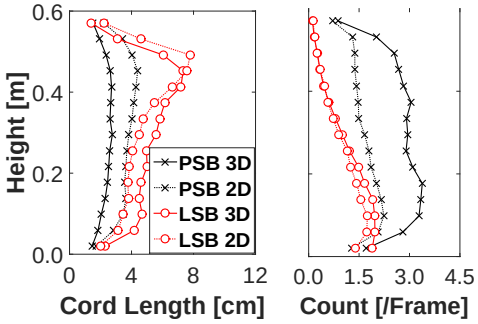

Figure 10: Comparison of time-averaged bubble cord length and count using 2D and 3D algorithms applied to lab-scale bed *LSB* (diameter = 14.5 cm) and pilot-scale bed *PSB* (diameter = 30 cm) for U/U_{mf}=4.6

U/U_{mf}=4.6. As in the LSB, volumetric bubble diameter increases with bubble growth and coalescence while the frequency (count) depreciates. As expected, the bubble diameters are significantly smaller than the corresponding values in Figure 7b primarily due to increased bed size and consequently, reduced slugging effects [30]. Interestingly, AR_1 and AR_2 profiles almost coincide indicating that, in general, bubbles are symmetric about their axes. Finally, average bubble velocities positively correlate with diameters, although there is a decreasing trend beyond y=0.4m since large bubbles (slugs) open to the free surface are not linked to avoid ambiguity. Even though similar-sized bubbles travel faster in large beds (due to lower wall effects [30]), the average bubble velocities here are slightly lower than the case of lab-scale bed (Figure 8b). This is because of the large fraction of small bubbles (< 3cm) which also travel much slower than the larger ones (bubble velocity is proportional to $\sqrt{d_b}$ [44]).

3.3. 2D statistics v/s 3D statistics

In this section, bubble statistics derived for both lab-scale bed (LSB) and pilot-scale bed (PSB) are compared using 2D and 3D (MS3DATA) detection, to highlight the limitations of the former. 2D statistics are essentially obtained by analyzing data on a single vertical slice of the bed while MS3DATA post-processes data from the entire bed. Figure 10 shows that for the case of U/U_{mf}=4.6, the disparity between 2D and 3D statistics is insignificant at the lab-scale but increases with bed diameter: average cord lengths predicted in PSB are almost 1.5× higher while bubble frequency is under-predicted by almost 2× when using 2D statistics. Even though 2D statistics are independent of the selected vertical slice (since averages are obtained over 27s), this approach may lead to considerable inaccuracies in bubble dynamics because (a) sizes of large bubbles and slugs are under-predicted (b) significant fraction of small bubbles is not detected and (c) azimuthal motion of bubbles cannot be quantified. Each of these limitations of 2D detection are discussed in detail below.

Figure 11 compares bubble statistics in PSB using large-bubble filter, i.e. only bubbles comparable to the bed diameter (cord length larger then 8 cm) are considered for averaging. While the detected bubble frequency is similar using both frameworks for this case, 2D detection considerably under-predicts the average cord length because the axes of individual bubbles (slugs) does not always align with the vertical slice used for computing

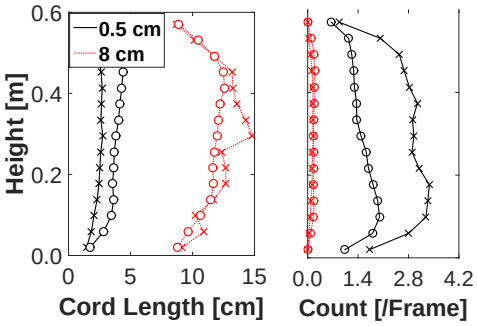

Figure 11: Comparison of time-averaged bubble diameter (cord length) and count (per frame) using small bubble filter (cord length >0.5cm) and large-bubble filter (cord length >8cm) with 3D (×) and 2D (○) bubble detection applied to PSB simulations for U/U_{mf}=4.6

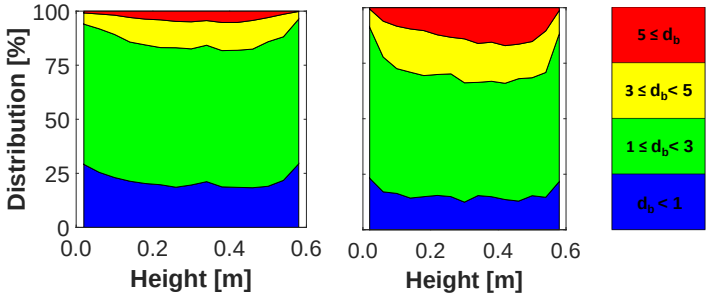

(a) 3D statistics (b) 2D statistics

Figure 12: Comparison of time-averaged cross-section normalized bubble size distribution using 2D and 3D bubble detection applied to PSB simulations for U/U_{mf}=4.6. Units for color legend is [cm]

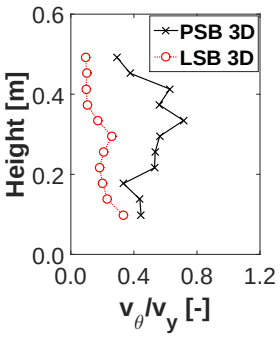

Figure 13: Time averaged tangential bubble velocity normalized by axial bubble velocity $|v_\theta|/(v_y)$ in LSB (diameter 14.5 cm) and PSB (diameter 30 cm) for U/U_{mf}=4.6. Only bubbles larger than 5 cm are retained for computing bubble velocities here.

bubble statistics. On the other hand, while using small-bubble filter (i.e. all bubbles larger than 0.5 cm are considered), average bubble sizes using 3D detection are considerably lower. This is because a significant fraction of small bubbles (especially smaller than 3 cm) is not detected for 2D statistics which is also evident from the cross-section normalized bubble distribution (i.e. the PDF of bubble size at different axial location) in PSB shown in Figure 12. In general, about 80% of the bubbles detected using 3D statistics are small (<3 cm) while this fraction is about 65% for 2D statistics indicating the lower likelihood of small bubbles getting detected using the latter. Overall, even though 2D statistics under-estimate large bubble sizes, bubble diameter predictions are still over-estimated (as observed in Figure 10) because of significantly lower fraction of small bubbles detected. These differences will only increase with increasing bed size.

Time-averaged bubble azimuthal velocities normalized with respect to the axial velocity $|v_\theta|/v_y$ are presented in Figure 13 for U/Umf=4.6 at both lab-scale and pilot-scale, with only large bubbles (>5cm) considered to highlight the significance of 3D linking. Since fluidization hydrodynamics are strongly influenced by bubble motion, $|v_\theta|/v_y$ is also representative of the swirl component in solids motion. As expected, bubbles predominantly move upwards through the bed center in thin lab-scale beds (low average $|v_\theta|/v_y$), while the azimuthal motion becomes significant (about 50% of the axial motion) in PSB. The disparity in profiles is expected to further increase with increasing gas velocity since on the one hand, bubble growth along the bed axis will be further aided in lab-scale beds while on the other hand, non-axial dispersion of gas momentum will increase in larger beds resulting in increased azimuthal motion [51].

Overall, differences in bubble statistics using 2D and 3D detection techniques are not surprising and this analysis shows that the former may actually suffice for small lab-scale beds (diameter < 15 cm). However, for larger-sized beds and/or fast fluidization conditions, the inherent limitations of 2D detection are escalated and consequent inaccuracies cannot be neglected. Further, this comparison also provides evidence regarding the inherent errors in experimental setups employing 2D measurement techniques for predicting bubble statistics (e.g. cord length predictions using optical probes could depend on measurement position and bubble trajectories), especially in large-scale beds. Note that the choice of the bubble statistics computing framework (2D/3D) must not be confused with the choice of underlying fluidization simulation i.e. this study investigates the comparison of 2D and 3D bubble statistics applied to 3D simulations. Under specific conditions, 3D cylindrical beds can be simulated using 2D Cartesian coordinates [51], however a comparison of 2D and 3D simulations is not the focus of this study.

3.4. Scalability of Bubble Statistics

Given the superior accuracy of 3D bubble statistics, especially for PSB simulations, this section evaluates the algorithm scalability by comparing the computational cost for the case of U/U_{mf}=4.6 in both LSB and PSB. For each case, the computational time is noted for three different grid resolutions (1×, 0.125× and 0.08× size(**A**) listed in Table 2), corresponding to grid resolutions 1.5-4 mm. Figure 14 shows the breakdown of average computational cost of bubble statistics for 2700 frames using Intel Core i7 3.5 GHz processor. While 2D bubble statistics are cheaper and can be obtained at approximately 0.01s per frame, 3D bubble statistics are significantly more expensive since these consider 80-160× more grid cells for PSB simulations.

All cases considered in Figure 14, including both 2D and 3D analyses, are collected and summarized in Figure 15. It may be inferred that the overall computational cost is almost equally split between numbering bubbles (Algorithm 1) and resolving conflicts (Algorithm 2). In general, the overall cost increases with both number of bubbles detected as well as grid resolution i.e. the number of cells in **A**. Although the total computational

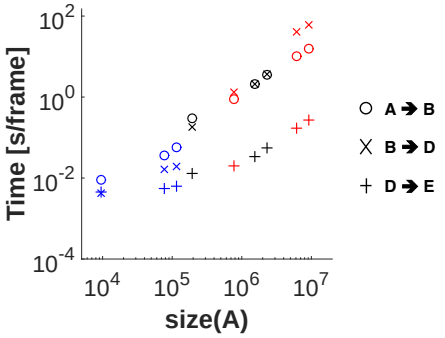

Figure 14: Computational time (per frame) for bubble detection **A**→**B** (∘), conflict resolution **B**→**D** (×) and property evaluation **D**→**E** (+) for different cases: PSB 2D (blue), LSB 3D (black) and PSB 3D (red). All cases are run for three different resolutions with size(**A**) representing the number of cells in **A**

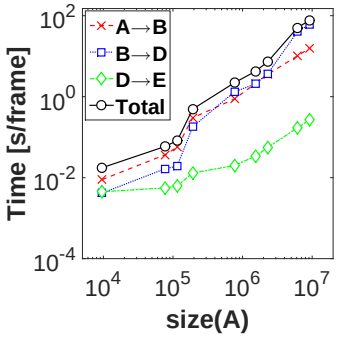

Figure 15: Summary of the computational time (per frame) for numbering bubbles (**A**→**B**), resolving conflicts (**B**→**D**) and evaluating property (**D**→**E**) for 2D and 3D statistics applied to LSB and PSB simulations. All cases are run for three different resolutions with size(A) representing the number of cells in **A**

time scales as a power law of the total grid cells (exponent 1.3), the total time required for bubble statistics is still less than 1% of the total simulation cost for the PSB case.

4. Conclusions

The performance of fluidized bed reactors is significantly dependent on the bubbling dynamics inside the bed. Accurately predicting bubble dynamics is essential for the qualitative description of the hydrodynamics as well as for predicting solids distribution and mixing. While lab-scale setups provide useful data for validation, there are severe limitations to characterize bubbles in larger beds. In this context, accurate description of bubbles using validated numerical simulations can complement experimental measurements at large scales and provide valuable insights into the hydrodynamics.

In this study, an algorithm for computing 3D bubble statistics using void fraction data from 3D CFD simulations is proposed. This algorithm detects bubbles by linking cells, links bubbles across successive frames and finally, evaluates bubble properties. MS3DATA is validated using analytical shapes as well as measurements from a lab-scale bed [18] and is subsequently, applied to pilot-scale bed of diameter 30 cm. It is shown that at large scale, there is significant error in bubble dynamics predicted using 2D statistics. By considering simulation data only along a vertical slice, 2D statistics significantly under-predict sizes of large bubbles while a large fraction of the small bubbles (<3 cm) is undetected. In addition, the lateral motion of bubbles becomes significant at these scales, unlike the case of lab-scale beds where bubbles move axially through the center, which cannot be captured using 2D statistics.

Finally, scalability of the algorithm is examined by considering 2D and 3D detection applied to both sized beds for different grid resolutions. 2D statistics are computed relatively fast ∼O(0.01 s/frame) while 3D statistics from highly resolved grids ($\sim 10^7$ cells) are significantly more expensive ∼O(90 s/frame) due to the large number of grid cells. For the cases presented, the computational cost increases as a power law of the number of grid cells (with exponent 1.3) used. While the algorithm could be further optimized, this cost is still

insignificant (<1%) as compared to the cost of accurate simulations at large-scale. Even though this study is focused on evaluating bubble dynamics in gas-solid fluidized beds at large-scales, the algorithm itself can be easily applied and extended for detecting bubbles, drops and clusters in other areas of 2D and 3D multiphase flows.

5. Acknowledgment

The authors gratefully acknowledge BP for funding this research. This research was supported in part by an appointment to the National Energy Technology Laboratory Research Participation Program, sponsored by the U.S. Department of Energy and administered by the Oak Ridge Institute for Science and Education.

References

[1] D. Kunii and O. Levenspiel. *Fluidization Engineering*. 1991.

[2] A. Bakshi, C. Altantzis, R.B. Bates, and A.F. Ghoniem. Eulerian-Eulerian simulation of dense solid-gas cylindrical fluidized beds: Impact of wall boundary condition and drag model on fluidization. *Powder Technology*, 277(0):47 – 62, 2015.

[3] C. Altantzis, R.B. Bates, and A.F. Ghoniem. 3D Eulerian modeling of thin rectangular gas-solid fluidized beds: Estimation of the specularity coefficient and its effects on bubbling dynamics and circulation times. *Powder Technology*, 270, Part A(0):256 – 270, 2015.

[4] P.N. Rowe, B.A. Partiridge, A.G. Cheney, G.A. Henwood, and E. Lyall. The mechanisms of solid mixing in fluidized beds. *Transactions of the Institute of Chemical Engineers*, 43:271–286, 1965.

[5] J. Baeyens and D. Geldart. Particle mixing in a gas fluidized bed. *La Fluidisation et ses applications*, pages 182–195, 1974.

[6] J. Werther. Convective solids transport in large diameter gas fluidized beds. *Powder Technology*, 15(2):155 – 167, 1976.

[7] T. Litka and L.R. Glicksman. The influence of particle mechanical properties on bubble characteristics and solid mixing in fluidized beds. *Powder Technology*, 42(3):231 – 239, 1985.

[8] M Stein, Y.L Ding, J.P.K Seville, and D.J Parker. Solids motion in bubbling gas fluidised beds. *Chemical Engineering Science*, 55(22):5291 – 5300, 2000.

[9] S. Sanchez-Delgado U. Ruiz-Rivas A. Soria-Verdugo, L.M. Garcia-Gutierrez. Circulation of an object imersed in a bubbling fluidized bed. *Chemical Engineering Science*, 66(1):78–87, 2011.

[10] N Kobayashi, R Yamazaki, and S Mori. A study on the behavior of bubbles and solids in bubbling fluidized beds. *Powder Technology*, 113(3):327 – 344, 2000.

[11] O. Oke, P. Lettieri, P. Salatino, R. Solimene, and L. Mazzei. Numerical simulations of lateral solid mixing in gas-fluidized beds. *Chemical Engineering Science*, 120(0):117 – 129, 2014.

[12] H.R. Norouzi, N. Mostoufi, Z. Mansourpour, R. Sotudeh-Gharebagh, and J. Chaouki. Characterization of solids mixing patterns in bubbling fluidized beds. *Chemical Engineering Research and Design*, 89(6):817 – 826, 2011.

[13] L. Shen, F. Johnsson, and B. Leckner. Digital image analysis of hydrodynamics two-dimensional bubbling fluidized beds. *Chemical Engineering Science*, 59(13):2607 – 2617, 2004.

[14] A. Busciglio, G. Vella, G. Micale and L. Rizzuti Analysis of the bubbling behavior of 2D gas solid fluidized beds. Part I. Digital Image analysis Technique. *Chemical Engineering Journal*, 140(0):398 – 413, 2008.

[15] S. Movahedirad, A. Molaei Dehkordi, M. Banaei, N. G. Deen, M. van Sint Annaland, and J. A. M. Kuipers. Bubble size distribution in two-dimensional gas-solid fluidized beds. *Industrial & Engineering Chemistry Research*, 51(18):6571–6579, 2012.

[16] M. Rüdisüli, T. J. Schildhauer, S. M.A. Biollaz, and J. Ruud van Ommen. Bubble characterization in a fluidized bed by means of optical probes. *International Journal of Multiphase Flow*, 41(0):56 – 67, 2012.

[17] C. Sobrino, A. Acosta-Iborra, D. Santana, and M. de Vega. Bubble characteristics in a bubbling fluidized bed with a rotating distributor. *International Journal of Multiphase Flow*, 35(10):970 – 976, 2009.

[18] M. Rüdisüli, T. J. Schildhauer, Serge M.A. Biollaz, Alexander Wokaun, and J. Ruud van Ommen. Comparison of bubble growth obtained from pressure fluctuation measurements to optical probing and literature correlations. *Chemical Engineering Science*, 74(0):266 – 275, 2012.

[19] M. Liu, Y. Zhang, H. Bi, J. R. Grace, and Y. Zhu. Non-intrusive determination of bubble size in a gas-solid fluidized bed: An evaluation. *Chemical Engineering Science*, 65(11):3485 – 3493, 2010.

[20] A. Acosta-Iborra, C. Sobrino, F. Hernndez-Jimnez, and M. de Vega. Experimental and computational study on the bubble behavior in a 3-d fluidized bed. *Chemical Engineering Science*, 66(15):3499 – 3512, 2011.

[21] J. Werther. Influence of the bed diameter on the hydrodynamics of gas-fluidized beds. *AIChE Symp. Series*, 70(141):53–64, 1974.

[22] C.E.J. van Lare, H.W. Piepers, J.N. Schoonderbeek, and D. Thoenes. Investigation on bubble characteristics in a gas fluidized bed. *Chemical Engineering Science*, 52(5):829 – 841, 1997.

[23] X. Yang M.C. Melaaen C. Rautenbach, R.F. Mudde and B.M. Halvorsen. A comparative study between electrical capacitance tomography and time-resolved x-ray tomography. *Flow Measurement and Instrumentation*, 30:34–34, 2013.

[24] I. Hulme and A. Kantzas. Determination of bubble diameter and axial velocity for a polyethylene fluidized bed using x-ray fluoroscopy. *Powder Technology*, 147(13):20 – 33, 2004.

[25] V. Verma, J. T. Padding, N. G. Deen, J. A. M. (Hans) Kuipers, F. Barthel, M. Bieberle, M. Wagner, and U. Hampel. Bubble dynamics in a 3-d gas-solid fluidized bed using ultrafast electron beam x-ray tomography and two-fluid model. *AIChE Journal*, 60(5):1632–1644, 2014.

[26] G.C. Brouwer, E.C. Wagner, J.R. van Ommen, and R.F. Mudde. Effects of pressure and fines content on bubble diameter in a fluidized bed studied using fast x-ray tomography. *Chemical Engineering Journal*, 207(0):711 – 717, 2012.

[27] C. M. Boyce, D. J. Holland, S. A. Scott, and J. S. Dennis. Adapting data processing to compare model and experiment accurately: A discrete element model and magnetic resonance measurements of a 3d cylindrical fluidized bed. *Industrial & Engineering Chemistry Research*, 52(50):18085–18094, 2013.

[28] T. W. Asegehegn, M. Schreiber, and H. J. Krautz. Influence of two- and three-dimensional simulations on bubble behavior in gassolid fluidized beds with and without immersed horizontal tubes. *Powder Technology*, 219(0):9 – 19, 2012.

[29] Y. Lu, J. Huang, and P. Zheng. A cfd-dem study of bubble dynamics in fluidized bed using flood fill method. *Chemical Engineering Journal*, 274(0):123 – 131, 2015.

[30] S. Karimipour and T. Pugsley. A critical evaluation of literature correlations for predicting bubble size and velocity in gassolid fluidized beds. *Powder Technology*, 205(13):1 – 14, 2011.

[31] C. Sobrino, A. Acosta-Iborra, M.A. Izquierdo-Barrientos, and M. de Vega. Three-dimensional two-fluid modeling of a cylindrical fluidized bed and validation of the maximum entropy method to determine bubble properties. *Chemical Engineering Journal*, (0):–, 2014.

[32] C. Sobrino, A. Acosta-Iborra, D. Santana, and M. de Vega. Bubble characteristics in a bubbling fluidized bed with a rotating distributor. *International Journal of Multiphase Flow*, 35(10):970 – 976, 2009.

[33] N. P. Franka and T. J. Heindel. Local time-averaged gas holdup in a fluidized bed with side air injection using x-ray computed tomography. *Powder Technology*, 193(1):69 – 78, 2009.

[34] A.T Harris, J.F Davidson, and R.B Thorpe. The prediction of particle cluster properties in the near wall region of a vertical riser (200157). *Powder Technology*, 127(2):128 – 143, 2002.

[35] N. Firuzian, R. Sotudeh-Gharebagh, and N. Mostoufi. Experimental investigation of cluster properties in dense gas-solid fluidized beds of different diameters. *Particuology*, 16(0):69 – 74, 2014.

[36] J. Aubin, M. Ferrando, and V. Jiricny. Current methods for characterising mixing and flow in microchannels. *Chemical Engineering Science*, 65(6):2065 – 2093, 2010.

[37] A. A. Kulkarni and J. B. Joshi. Bubble formation and bubble rise velocity in gas-liquid systems: a review. *Industrial & Engineering Chemistry Research*, 44(16):5873–5931, 2005.

[38] J.M. van Baten and R. Krishna. Eulerian simulations for determination of the axial dispersion of liquid and gas phases in bubble columns operating in the churn-turbulent regime. *Chemical Engineering Science*, 56(2):503 – 512, 2001. 16th International Conference on Chemical Reactor Engineering.

[39] F. Sarrazin, K. Loubire, L. Prat, C. Gourdon, T. Bonometti, and J. Magnaudet. Experimental and numerical study of droplets hydrodynamics in microchannels. *AIChE Journal*, 52(12):4061–4070, 2006.

[40] M Bieberle, E Schleicher, and U Hampel. Simulation study on electron beam x-ray ct arrangements for two-phase flow measurements. *Measurement Science and Technology*, 19(9), 2008.

[41] J. Belden, S. Ravela, T. T. Truscott, and A. H. Techet. Three-dimensional bubble field resolution using synthetic aperture imaging: application to a plunging jet. *Experiments in Fluids*, 53(3):839–861, 2012.

[42] R Thorn, G A Johansen, and B T Hjertaker. Three-phase flow measurement in the petroleum industry. *Measurement Science and Technology*, 24(1):012003, 2013.

[43] A. Bakshi, C. Altantzis, and A.F. Ghoniem. Towards accurate three-dimensional simulation of dense multi-phase flows using cylindrical coordinates. *Powder Technology*, 264(0):242 – 255, 2014.

[44] S. Mori and C.Y. Wen. Estimation of the bubble diameter in gaseous fluidized beds. *AIChE Journal*, 21:109–115, 1975.

[45] D.G. Schaeffer. Instability in the evolution equations describing incompressible granular flow. *Journal of Differential Equations*, 66:19–50, 1987.

[46] J. Ding and D. Gidaspow. A bubbling fluidization model using kinetic theory of granular flow. *AIChE Journal*, 36(4):523–538, 1990.

[47] M. Syamlal, W. Rogers, and T. J. O'Brien. *MFIX Documentation Theory Guide*, 1993.

[48] P.C. Johnson and R. Jackson. Frictional-collisional constitutive relations for granular materials, with application to plane shearing. *J. Fluid Mech.*, 176:67–93, 1987.

[49] T. Li and S. Benyahia. Revisiting Johnson and Jackson boundary conditions for granular flows. *AIChE Journal*, 58(7):2058–2068, 2012.

[50] M. Syamlal. *MFIX Documentation Numerical Technique*, January 1998.

[51] N. Xie, F. Battaglia, and S. Pannala. Effects of using two- versus three-dimensional computational modeling of fluidized beds: Part ii, budget analysis. *Powder Technology*, 182(1):14 – 24, 2008.